



HAL
open science

Landau Theory for Non-Symmetry-Breaking Electronic Instability Coupled to Symmetry-Breaking Applied to Prussian Blue Analogue

Giovanni Azzolina, Roman Bertoni, Claude Ecolivet, Hiroko Tokoro, Shin-Ichi Ohkoshi, Eric Collet

► **To cite this version:**

Giovanni Azzolina, Roman Bertoni, Claude Ecolivet, Hiroko Tokoro, Shin-Ichi Ohkoshi, et al.. Landau Theory for Non-Symmetry-Breaking Electronic Instability Coupled to Symmetry-Breaking Applied to Prussian Blue Analogue. *Physical Review B*, 2020, 102 (13), 10.1103/PhysRevB.102.134104. hal-02964126

HAL Id: hal-02964126

<https://hal.science/hal-02964126>

Submitted on 12 Oct 2020

HAL is a multi-disciplinary open access archive for the deposit and dissemination of scientific research documents, whether they are published or not. The documents may come from teaching and research institutions in France or abroad, or from public or private research centers.

L'archive ouverte pluridisciplinaire **HAL**, est destinée au dépôt et à la diffusion de documents scientifiques de niveau recherche, publiés ou non, émanant des établissements d'enseignement et de recherche français ou étrangers, des laboratoires publics ou privés.

Landau Theory for Non-Symmetry-Breaking Electronic Instability Coupled to Symmetry-Breaking Applied to Prussian Blue Analogue

Giovanni Azzolina,¹ Roman Bertoni,¹ Claude Ecolivet,¹ Hiroko Tokoro,² Shin-ichi Ohkoshi,³ Eric Collet*¹

¹ Univ Rennes, CNRS, IPR (Institut de Physique de Rennes) - UMR 6251, F-35000 Rennes, France

² Division of Materials Science, Faculty of Pure and Applied Sciences, Univ Tsukuba, 1-1-1 Tennodai, Tsukuba, Ibaraki 305-8577, Japan.

³ Department of Chemistry, School of Science, The University of Tokyo, 7-3-1 Hongo, Bunkyo-ku, Tokyo 113-0033, Japan.

E-mail: eric.collet@univ-rennes1.fr

Abstract: Different types of ordering phenomena may occur during phase transitions, described within the universal framework of the Landau theory through the evolution of one, or several, symmetry-breaking order parameter η . In addition, many systems undergo phase transitions related to an electronic instability, in the absence of a symmetry-breaking and eventually described through the evolution of a totally symmetric order parameter q linearly coupled to volume change. Analyzing the coupling of a non-symmetry-breaking electronic instability, responsible for volume strain, to symmetry-breaking phenomena is of importance for many systems in nature and here we show that the symmetry-allowed $q\eta^2$ coupling plays a central role. We use as case study the rubidium manganese hexacyanoferrate Prussian blue analogue, exhibiting phase transitions with hysteresis that may exceed 100 K, and based on intermetallic charge transfer (CT). During the phase transition, the intermetallic CT described through the evolution of q is coupled to cubic-tetragonal ferroelastic symmetry-breaking described through the evolution of η . In this system, the symmetry-breaking and non-symmetry breaking deformations have similar amplitudes but the large volume strain is mainly due to CT. We analyze both the ferroelastic and the CT features of the phase transition within the frame of the Landau theory, taking into account the $q\eta^2$ coupling, stabilizing concomitant CT and Jahn-Teller distortion. The results show that the phase transition and its wide thermal hysteresis originate from the coupling between both processes and that the elastic coupling of each order parameter with the volume strain is responsible for the $q\eta^2$ coupling. The phase diagrams obtained with this model are in good qualitative agreement with various experimental findings and apply to diverse families of materials undergoing Mott transition, spin-crossover, neutral-ionic transition..., for which isostructural electronic instability driving volume strain can couple to symmetry-breaking or not, create phase transition lines and drive cooperative phenomena.

PACS: 64.60.-I, 62.20.D-, 61.50.Ks, 64.70.K-

I. Introduction

Phase transitions in materials are responsible for the emergence of physical properties, which is one of the main topics in condensed matter physics, and understanding their origin is of central interest for material science. The Landau theory of phase transitions¹ is a universal concept describing, through the evolution of a symmetry-breaking order parameter (OP) η , various types of ordering phenomena like ferromagnetic, ferroelectric, ferroelastic or other types of structural and/or electronic orders. In addition, many systems do not fit in this scheme as they may undergo phase transitions related to an electronic instability in the absence of symmetry-breaking. For example, this is the case of some charge-transfer (CT) systems, spin-crossover materials, Mott or insulator-metal transitions systems.²⁻¹³ These non-symmetry-breaking phase transitions may be described through the evolution of an order parameter q , related to an electronic instability, which transforms as the identity representation and is consequently responsible for a volume strain v_s due to the relative change of the bonding or antibonding nature of the electronic distribution. Different types of instabilities may couple during phase transitions. In addition to multiferroic materials, where different types of orders compete,¹⁴ there are other systems for which the non-symmetry-breaking change of electronic state may couple to a symmetry-breaking structural distortion. In this case, the symmetry-allowed $q\eta^2$ coupling term of lowest order plays a central role, as experimentally or theoretically explained in few cases.¹⁵⁻²¹ In this paper, we use the Landau theory approach to underline the key role of the volume strain related to a non-symmetry-breaking electronic instability q , which may couple to a symmetry-breaking instability η . We show that the $q\eta^2$ coupling of elastic nature increases the hysteresis regime of bistability. The variety of phase diagrams obtained with this model can apply to diverse systems undergoing non-symmetry-breaking and symmetry-breaking instabilities that may occur simultaneously or sequentially.

As a case study, we investigate the phase transition in rubidium manganese hexacyanoferrate (RbMnFe) Prussian blue analogue (PBA). The materials belong to the family of cyano-bridged metal complexes exhibiting switching of physical properties controlled by various external parameters including temperature, pressure, light or electric fields,^{9, 22-26} resulting from coupled intermetallic CT and structural reorganizations. These bistable PBA, with general composition $\text{Rb}_x\text{Mn}[\text{Fe}(\text{CN})_6]_{(x+2)/3} \cdot z\text{H}_2\text{O}$, undergo a CT-based thermal phase transition^{27, 28} between a high-temperature (HT) cubic phase $\text{Fe}^{\text{III}}(S = 1/2)\text{-CN-Mn}^{\text{II}}(S = 5/2)$ and a low-temperature (LT) tetragonal phase $\text{Fe}^{\text{II}}(S = 0)\text{-CN-Mn}^{\text{III}}(S = 2)$ (Fig. 1). The associated thermal hysteresis, probed by magnetic measurements (Fig. 2), may reach up to 138 K for some systems. This phase transition involves two types of instabilities: the non-symmetry-breaking CT and the ferroelastic distortion.

On the one hand, the CT bistability was theoretically described in terms of the Slichter-Drickamer or Ising models,^{29, 30} which did not account for the ferroelastic symmetry-breaking. On the other hand, the cubic-tetragonal ferroelastic distortion was deeply investigated in many systems,³¹⁻³⁶ and especially the associated volume and tetragonal distortion strains. For RbMnFe, periodic DFT methods provided also correct description of the equilibrium structures of the different electronic configurations.³⁷ However, there are several properties of RbMnFe like the change of magnetic susceptibility or the ferromagnetic order at low temperature,³⁸ that can only be explained by taking into account both the ferroelastic distortion, responsible for magnetic anisotropy, and the CT, responsible for the change of spin state. The CT process induces an important volume strain (10%), mediated by the cyano-bridges through the lattice, responsible for cooperative phase transitions, also observed for non-symmetry-breaking CT-based phase transitions.^{4-10, 39} Our analysis sheds a new light on the interpretation of experimental data on the sample RbMn[Fe(CN)₆],^{27, 40-42} and shows that both the non-symmetry-breaking CT (q) and ferroelastic symmetry-breaking distortion (η) must be considered on an equal footing.

The paper is organized as follows. In Sec. II we discuss experimental fingerprints of the phase transition in RbMnFe in terms of the symmetry-breaking structural distortion and the non-symmetry-breaking CT process. In Sec. III we present the Landau theory of the ferroelastic and the CT instabilities, and their symmetry-allowed $q\eta^2$ coupling, with a comprehensive analysis of the phase diagrams, and show that this coupling opens a phase transition line and broadens the thermal hysteresis. In Sec. IV we discuss both theoretical and experimental results and the important role of the elastic coupling for RbMnFe materials. In Sec. V we conclude on the work and the interest of our generic phase diagram, which can apply for describing various types of systems, for which the coupling between non-symmetry-breaking electronic instability and symmetry-breaking structural order is the key for explaining the emergence of functions.

II Experimental study of the RbMnFe PBA

Rb_xMn[Fe(CN)₆]_{(x+2)/3}·zH₂O, exhibits bistability between two phases with different structural and electronic configurations (Fig. 1).²⁸ The high temperature (HT) phase with a high entropy forms a FCC lattice with metals in O_h ligand fields and an electronic configuration Mn^{II}(S=5/2)Fe^{III}(S=1/2). The low temperature (LT) phase is tetragonal, as Jahn-Teller (JT) distortion stabilizes the Mn^{III}(S=2)Fe^{II}(S=0) state with empty Mn(dx²-y²) orbital, with metals being in D_{4h} ligand fields.⁴³ Various techniques described the occurrence of Fe-to-Mn CT-based phase transition from LT to HT phases at thermal equilibrium, or under light irradiation.^{23, 44, 45}

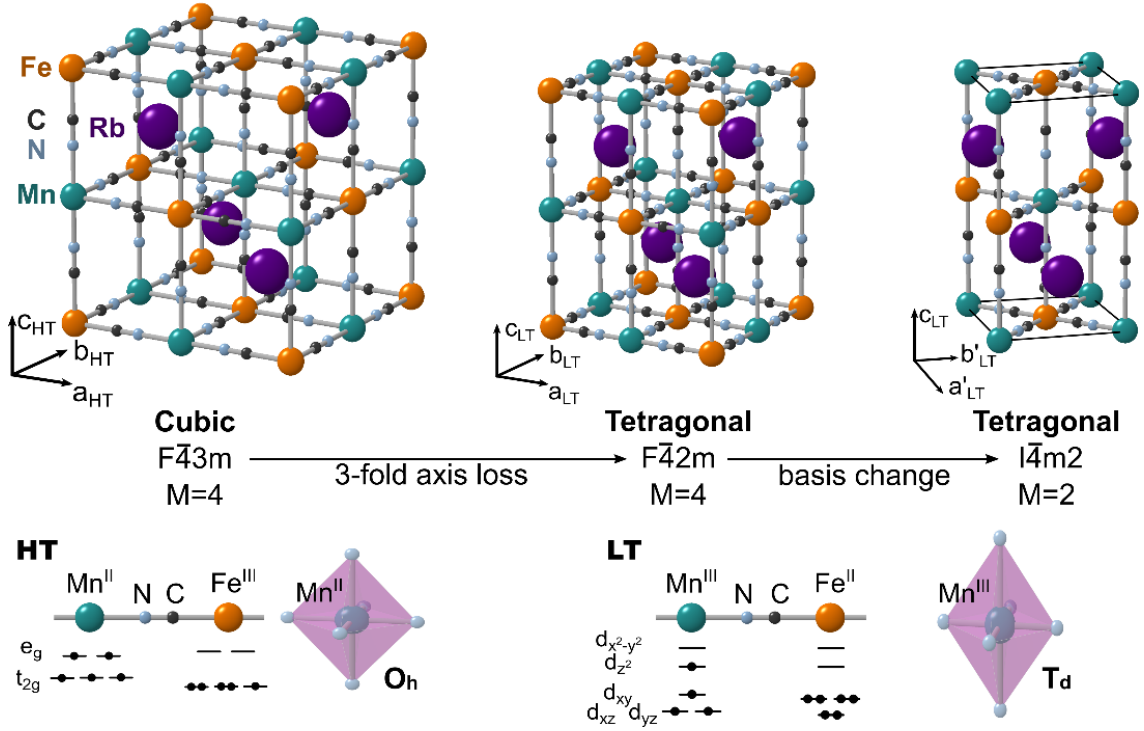


FIG. 1. Structures of the $\text{Mn}^{\text{II}}\text{Fe}^{\text{III}}$ HT phase ($F\bar{4}3m$), and $\text{Mn}^{\text{III}}\text{Fe}^{\text{II}}$ LT phase ($F\bar{4}2m$). Mn, N, C, Fe and Rb are shown in green, light blue, black, orange and purple respectively. The conventional $I\bar{4}m2$ LT space group is equivalent to the $F\bar{4}2m$ for which the (a_{LT}, b_{LT}, c_{LT}) cell corresponds to the HT one. The representation of the electronic configurations in the LT and HT phases show that the O_h ligand field stabilizes the Mn^{II} state, while the Mn^{III} state is stabilized by JT distortion splitting occupied d_{z^2} and unoccupied $d_{x^2-y^2}$ orbitals.

As a case study, we discuss the experimental fingerprints of the phase transition for the $\text{RbMn}[\text{Fe}(\text{CN})_6]$ system. The thermal dependence of its $\chi_M T$ product (molar magnetic susceptibility χ_M and temperature T) is shown in Fig. 2.^{27, 40-42} Upon warming, the $\chi_M T$ value characteristic of the $\text{Mn}^{\text{III}}(\text{S}=2)\text{Fe}^{\text{II}}(\text{S}=0)$ LT state increases around $T_u = 304$ K to reach a value characteristic of the $\text{Mn}^{\text{II}}(\text{S}=5/2)\text{Fe}^{\text{III}}(\text{S}=1/2)$ state. Upon cooling from the HT phase the $\chi_M T$ value suddenly drops around $T_d = 231$ K, resulting in a wide thermal hysteresis loop ($T_u - T_d = 73$ K). Similar first-order phase transitions were observed for various chemical compositions, and the Rb concentration acts as a chemical control of the hysteresis width, which reaches up to 138 K for $\text{Rb}_{0.64}\text{Mn}[\text{Fe}(\text{CN})_6]_{0.88}1.7\text{H}_2\text{O}$. The $\chi_M T$ evolution is usually described through the thermal population of the fraction γ of $\text{Mn}^{\text{II}}\text{Fe}^{\text{III}}$ HT state or the order parameter q :

$$\gamma = \frac{N_{\text{Mn}^{\text{II}}\text{Fe}^{\text{III}}}}{N_{\text{Mn}^{\text{II}}\text{Fe}^{\text{III}}} + N_{\text{Mn}^{\text{III}}\text{Fe}^{\text{II}}}} \quad \text{and} \quad q = \frac{N_{\text{Mn}^{\text{II}}\text{Fe}^{\text{III}}} - N_{\text{Mn}^{\text{III}}\text{Fe}^{\text{II}}}}{N_{\text{Mn}^{\text{II}}\text{Fe}^{\text{III}}} + N_{\text{Mn}^{\text{III}}\text{Fe}^{\text{II}}}}$$

$N_{\text{Mn}^{\text{II}}\text{Fe}^{\text{III}}}$ and $N_{\text{Mn}^{\text{III}}\text{Fe}^{\text{II}}}$ denote the number of sites in each CT states and $\gamma = \frac{q+1}{2}$. In the fully $\text{Mn}^{\text{II}}\text{Fe}^{\text{III}}$ phase $q = 1$, while in the fully $\text{Mn}^{\text{III}}\text{Fe}^{\text{II}}$ phase $q = -1$ (Fig. 2).

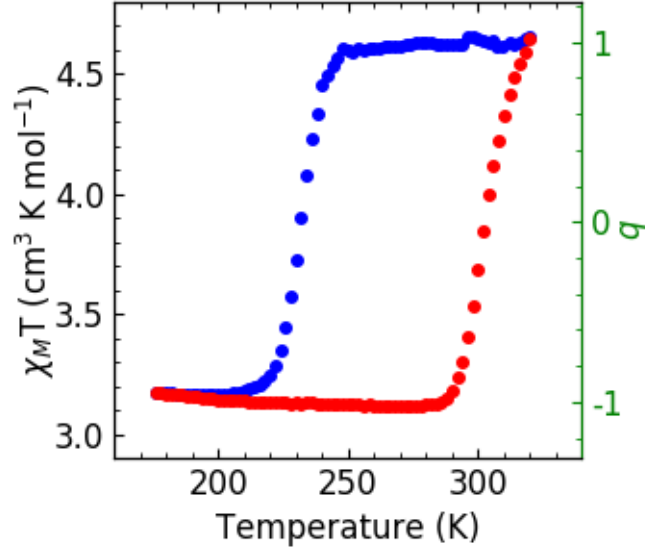


FIG. 2. $\chi_M T$ vs T plot characterizing the CT-based phase transition between the $\text{Mn}^{\text{III}}(\text{S}=2)\text{Fe}^{\text{II}}(\text{S}=0)$ LT phase and the HT $\text{Mn}^{\text{II}}(\text{S}=5/2)\text{Fe}^{\text{III}}(\text{S}=1/2)$ phase, revealing a ≈ 73 K wide thermal hysteresis.

X-ray and neutron diffraction studies revealed important structural changes of the 3D polymeric network during the CT-based phase transition.^{40,46} The space group of the HT cubic phase is $F\bar{4}3m$ ($Z=4$) with a lattice parameter $a_{\text{HT}} \approx 10.56$ Å. A symmetry-breaking occurs in the LT phase, with a tetragonal cell usually described in the conventional space group $I\bar{4}m2$ ($Z=2$ $a_{\text{LT}}' = b_{\text{LT}}' \approx 7.09$ Å and $c_{\text{LT}} \approx 10.52$ Å). Here, we use the equivalent and non-conventional $F\bar{4}2m$ cell, for which the lattice vectors corresponds to the ones of the HT lattice. The lattice vectors (Fig. 1) of the $F\bar{4}2m$ ($Z=4$) and $I\bar{4}m2$ space groups are related by: $a_{\text{LT}} = (a_{\text{LT}}' - b_{\text{LT}}')$ and $a_{\text{LT}} = (a_{\text{LT}}' + b_{\text{LT}}')$, with $a_{\text{LT}} \approx 10.02$ Å. Fig. 3 shows the evolution of the lattice parameters for $\text{RbMn}[\text{Fe}(\text{CN})_6]$.⁴⁰ The ferroelastic distortion from cubic $F\bar{4}3m$ to tetragonal $F\bar{4}2m$ space groups results in a splitting of the lattice parameter a_{HT} into a_{LT} and c_{LT} . The structural instability occurs at the Γ point of the Brillouin zone and the symmetry-breaking OP η belongs to the unique bidimensional E representation of the $\bar{4}3m$ point group. These nano-crystals are single domain, as in the low temperature phase there is not splitting of the Bragg peak measured on an oriented film⁴⁶.

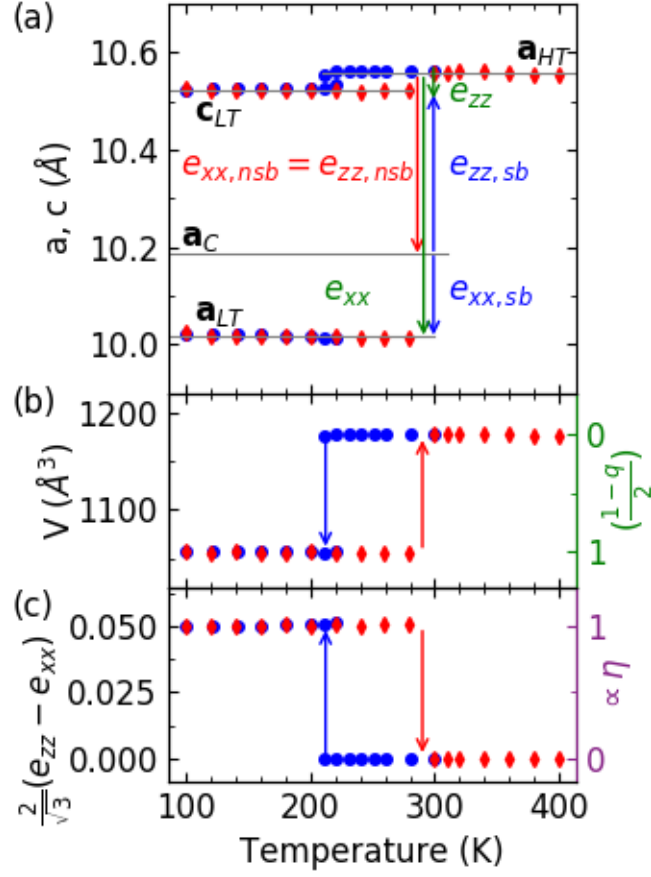


FIG. 3. (a) Thermal evolution of the lattice parameters between HT and LT phases. The solid lines mark the average values in each phase. The vertical arrows refer to structural changes corresponding to non-symmetry-breaking ($nsb \equiv q$) and the symmetry-breaking ($sb \equiv \eta$) components. (b) Volume change scaled to $\frac{1-q}{2}$ (right axis). (c) Thermal evolution of the ferroelastic distortion $\frac{2}{\sqrt{3}}(e_{zz} - e_{xx}) \propto \eta$ (arbitrarily scaled to 1).

For cubic-tetragonal phase transitions,^{33, 36, 47} two strain parameters are involved:

i) the ferroelastic cubic-tetragonal distortion strain corresponding to the symmetry-breaking OP

$$\eta \propto \frac{1}{\sqrt{3}}(2e_{zz} - e_{xx} - e_{yy}) = \frac{2}{\sqrt{3}}(e_{zz} - e_{xx}),$$

monitoring deviation from the cubic symmetry (Fig. 3a) of the LT lattice^{35, 48}, with the total deformations measured during the phase transition

$$e_{xx} = \frac{a_{LT} - a_{HT}}{a_{HT}}, \quad e_{zz} = \frac{c_{LT} - a_{HT}}{a_{HT}},$$

ii) the volume strain $v_s(T) = \frac{V_{LT}(T) - V_{HT}(T)}{V_{HT}(T)},$

The indexes "HT" refer to the value of the HT parameters extrapolated at low temperature by a linear fit as suggested by the thermal evolution. For purely ferroelastic phase transitions, the single symmetry-breaking does not contribute to v_s in a first approximation, as the first order components of the spontaneous strain tensors distortion correspond to $v_s = e_{xx} + e_{yy} + e_{zz} = 0$. Fig. 3b shows the large volume jump ($v_s \approx 0.1$) during the phase transition between the HT and LT

phases. It corresponds to an average variation of the lattice parameter $\Delta a = a_{HT} - a_c = 0.37 \text{ \AA}$, with $a_c = (2a_{LT} + c_{LT})/3$. The amplitude of this non-symmetry-breaking distortion is similar to the symmetry-breaking ferroelastic distortion, splitting of the lattice parameters with $c_{LT} - a_{LT} = 0.54 \text{ \AA}$. Therefore, both symmetry-breaking and non-symmetry-breaking deformations must be considered on an equal footing. This deformation of the lattice translates in the structural deformations within the unit cell, as observed upon warming for example (Fig. 4). The structural analysis evidenced the splitting of the six Mn-N bonds, equivalent in the HT phase, into four shorter ($d_s \approx 1.89 \text{ \AA}$ along x and y) and two longer ones ($d_l \approx 2.29 \text{ \AA}$ along z) in the LT phase due to the JT distortion.^{27, 40-42, 45} In addition, the average bond length $\langle \text{Mn-N} \rangle$ decreases from HT to LT due to the less bonding nature of the HT Mn^{II} state with two electrons on the e_g orbitals. Here again, the amplitude of the splitting of the Mn-N bond lengths scales with the symmetry-breaking components ($\propto \eta$), while the average bond length change $\Delta \langle \text{Mn-N} \rangle$ corresponds to non-symmetry breaking components q ($\propto \gamma$). Similar changes occurs on the Fe-C bonds, with a weaker splitting.

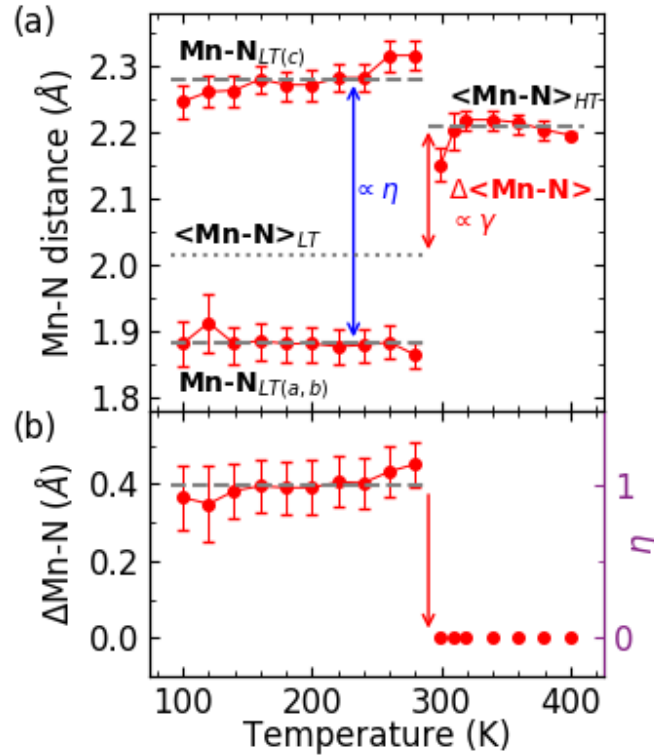


FIG. 4. The structural deformations at the atomic scale within the unit cell. In the HT phase the six Mn-N bonds are equivalent, while in the LT phase there are four short ($d_s \approx 1.89 \text{ \AA}$ along x and y) and two long ($d_l \approx 2.29 \text{ \AA}$ along z) bonds. The splitting $\Delta \text{Mn-N}$ of the bond lengths relates to symmetry-breaking components ($\propto \eta$) and the jump $\Delta \langle \text{Mn-N} \rangle$ of the average bond length to non-symmetry-breaking components q ($\propto \gamma$).

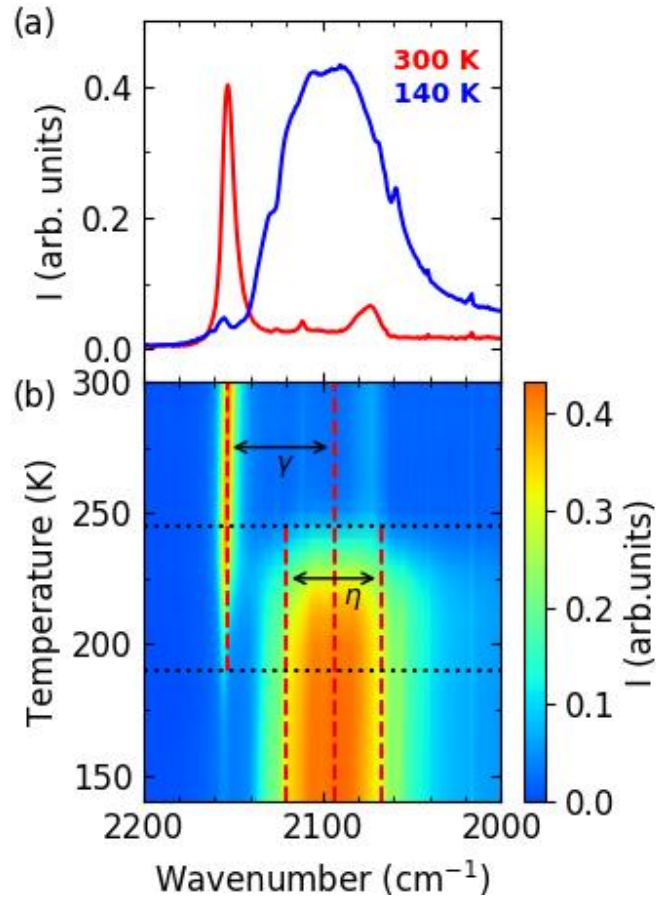


FIG. 5. Temperature dependence of the C-N stretching mode of the IR spectrum. At HT the 6 C-N bonds are equivalent, corresponding to a single stretching mode observed around 2150 cm^{-1} . In the LT phase the band shifts around 2090 cm^{-1} is due to the non-symmetry-breaking change of electronic state q ($\propto \gamma$) and it broadens due to the splitting of the CN modes related to the symmetry-breaking ($\propto \eta$).

The coupled symmetry-breaking and change of electronic state also translate in IR data. Fig. 5 shows the temperature dependence of the C-N stretching mode in the cooling mode.²⁷ In the HT phase, the six C-N bonds are equivalent with a single stretching mode observed at $\approx 2150 \text{ cm}^{-1}$. In the LT phase, the band shifts around 2090 cm^{-1} as CT increases the bonding strength, and splits as symmetry-breaking generates inequivalent C-N bonds. The broad LT band includes then several modes due to degeneracy lifting. Here again, the splitting of the CN modes broadening the LT IR band is due to the symmetry-breaking component ($\propto \eta$) and the average frequency jump is due to the non-symmetry-breaking component related to the change of electronic state q ($\propto \gamma$).

To summarize, various experimental results reveal that the changes observed during the phase transition include symmetry-breaking and non-symmetry-breaking components, which simultaneously change during the phase transition, with similar amplitudes. Hereafter, we develop a theoretical model based on the Landau theory to describe the phase transition, by taking into account both aspects to understand the origin of the large thermal hysteresis domain of bistability.

III. Landau analysis of the phase transition

A. Landau development for the purely ferroelastic phase transition

The cubic-tetragonal ferroelastic transition corresponds to the symmetry change from the cubic space group $F\bar{4}3m$ to the non-conventional tetragonal space group $F\bar{4}2m$ (Fig. 1). Since the structural instability occurs at the Γ point of the Brillouin zone, the phase transition is described by considering the group-subgroup relationship between the $\bar{4}3m$ and $\bar{4}2m$ point groups. As noticed above, the symmetry-breaking OP η belongs then to the bidimensional E representation of the $\bar{4}3m$ point group, the basis of which is built with two distortion strains: the orthorhombic strain (e_o) and the tetragonal strain (η). In the case of the cubic-tetragonal ferroelastic transition, the orthorhombic strain $e_o = e_{xx} - e_{yy} = 0$. The bidimensional symmetry-breaking OP η obeys to the transformation properties ($2z^2 - x^2 - y^2$) of the JT mode,^{33, 36, 47, 49} with an anisotropic elongation along c and contraction along a and b (Fig. 3). We use the scalar η defined above as $\eta \propto (2e_{zz} - e_{xx} - e_{yy})$ in the simplest Landau development of the thermodynamic potential for the cubic-tetragonal transformation^{36, 48-51} truncated to the 4th order in η :

$$F = \frac{1}{2}a\eta^2 + \frac{1}{3}b\eta^3 + \frac{1}{4}c\eta^4$$

with $a = a_0(T - T_F)$ ($a_0 > 0$). We use $b < 0$ for stabilizing the JT elongation, while $c > 0$ stabilizes the tetragonal orientation along the principal directions,^{36, 49} resulting in 3 equivalent domains elongated along c , a or b . The stability of the different phases is found from $\frac{dF}{d\eta} = 0$ and $\frac{d^2F}{d\eta^2} > 0$.

$\eta = 0$ is stable for $a > 0$ ($T > T_F$), while $\eta = \frac{(-b + \sqrt{(b^2 - 4ac)})}{2c}$ is stable below $T_2 = T_F + \frac{b^2}{4ca_0}$. Both the analytical and numerical (Fig. 6a) studies from this model illustrate common trends of cubic-tetragonal ferroelastic transitions: the phases coexist in the $[T_F - T_2]$ range and the amplitude of η changes discontinuously, as the symmetry-allowed η^3 term in the development of the Landau potential is responsible for the first-order nature of the phase transition.⁴⁸

Figs. 7 shows the strongly first-order nature of the transition. However, the thermal evolution of η (and v_s), remaining almost constant in the LT phase, cannot be represented by the standard solutions of the potential for first-order phase transitions. In addition, $e_{xx} \approx -0.0511$ and $e_{zz} \approx -0.0038$ do not obey the conditions for cubic-tetragonal distortion, $2e_{xx} = 2e_{yy} = -e_{zz}$,^{33, 36, 47} which merits closer inspection. The volume of the LT phase is $V_{LT} = a_{LT}^2 c_{LT} \approx 1054.9 \text{ \AA}^3$, while the average ‘‘cubic’’ LT lattice with parameter a_c corresponds to the volume $V_c = a_c^3 \approx 1055.7 \text{ \AA}^3$. Therefore, the volume difference ($V_{LT} - V_c \approx -0.8 \text{ \AA}^3$) due to the ferroelastic symmetry-breaking only is much smaller than the volume change ($V_{HT} - V_{LT} \approx -121 \text{ \AA}^3$) between the HT and LT

phases. Therefore, the conventional Landau theory of cubic-tetragonal phase transition with a single ferroelastic order parameter is not sufficient for understanding the phase transition and the large v_s in RbMnFe, and the contribution from another order parameter must be questioned.

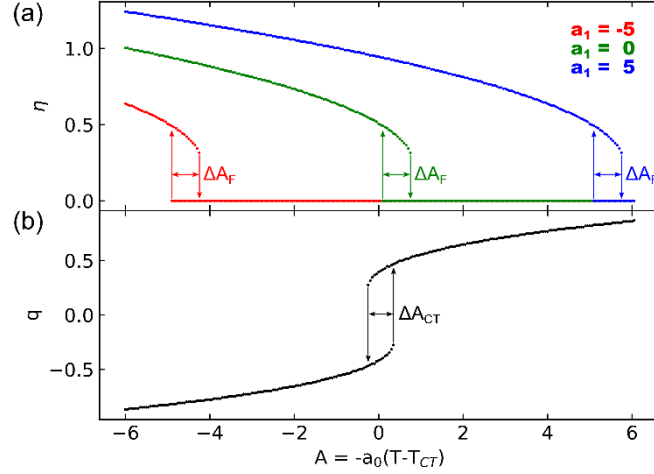


FIG. 6. Temperature dependence along A of uncoupled ($D=0$) order parameters η and q . a) Thermal evolution of the equilibrium value of the symmetry-breaking order parameter η for $a_I = -5, 0$ and $+5$. The width of the coexistence region between $\eta > 0$ and $\eta = 0$ is ΔA_F . b) The equilibrium evolution of q describes the CT transition curve and the width of the coexistence region between $q > 0$ and $q < 0$ is ΔA_{CT} . When $D=0$, the behavior of q is unchanged with a_I , which only shifts the relative position of T_F with respect to T_{CT} . ΔA_{CT} and ΔA_F are similar with the parameters used ($a_0=0.1$, $T_F=200$, $\frac{b}{3} = -2$, $\frac{c}{4} = 3$, $\frac{B}{2} = -1$, $\frac{C}{4} = 3$, $T_{CT}= 200$).

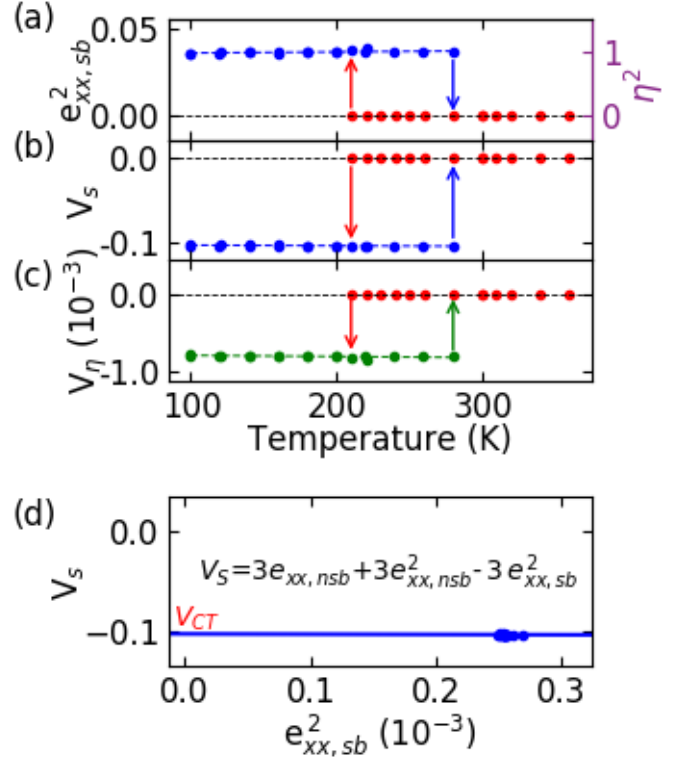
In the family of cyanide-bridged bimetallic systems, including non-symmetry-breaking CT-based phase transitions, the volume change is known to be due to the CT process, which modifies the population of antibonding e_g -like orbitals,^{4-10, 46} but which does not break symmetry. As explained by Carpenter,⁵² in such a case it is necessary to express the total strain due to the phase transition as the sum of two tensors: $[e] = [e_{sb}] + [e_{nsb}]$. $[e_{sb}]$ is the strain related to symmetry-breaking deformations, and $[e_{nsb}]$ is the strain related to non-symmetry-breaking deformations proportional to a unity matrix. Since $[e_{sb}]$ transforms as the irreducible representation E of the HT $\bar{4}3m$ point group and $[e_{nsb}]$ transforms as the identity representation, we must consider the following relationships between the components of the tensors:

$$\begin{bmatrix} e_{xx} & 0 & 0 \\ 0 & e_{xx} & 0 \\ 0 & 0 & e_{zz} \end{bmatrix} = \begin{bmatrix} e_{xx, sb} & 0 & 0 \\ 0 & e_{xx, sb} & 0 \\ 0 & 0 & -2e_{xx, sb} \end{bmatrix} + \begin{bmatrix} e_{xx, nsb} & 0 & 0 \\ 0 & e_{xx, nsb} & 0 \\ 0 & 0 & e_{xx, nsb} \end{bmatrix}$$

With $e_{xx, nsb} = \frac{1}{3}(2e_{xx} + e_{zz})$ and $e_{xx, sb} = \frac{1}{3}(e_{xx} - e_{zz})$.

Typical values $a_{HT} = 10.56 \text{ \AA}$, $a_{LT} = 10.02 \text{ \AA}$, $c_{LT} = 10.52 \text{ \AA}$ correspond to $e_{xx} = -0.0511$, $e_{zz} = -0.0038$, $e_{xx, nsb} = e_{zz, nsb} = -0.0353$, $e_{xx, sb} = -0.0158$, $e_{zz, sb} = 0.0315$.

FIG. 7. Symmetry-adapted strains calculated from the lattice parameters shown in Fig. 3. The cubic-tetragonal distortion strain $\eta^2 \propto e_{xx, sb}^2$ (a), the total volume strain v_s (b) and the symmetry-breaking volume strain v_η (c). (d) The strain–strain relationship between v_s and $e_{xx, sb}^2$ (d) has an affine nature and is mainly due to nsb deformations.



As shown in Fig. 3a, $e_{xx, nsb}$ describes the average lattice parameter change from a_{HT} to a_c , while $e_{xx, sb}$ describes the lattice parameter change from a_c to a_{LT} .

The ferroelastic distortion strain is $\frac{c(T)-a(T)}{a_{HT}(T)} = \frac{2}{\sqrt{3}}(e_{zz, sb} - e_{xx, sb}) = -\frac{6}{\sqrt{3}}(e_{xx, sb}) \propto \eta$, with

$$e_{xx, sb} = e_{yy, sb} = \frac{a(T)-a_c(T)}{a_{HT}(T)}, \quad e_{zz, sb} = \frac{c(T)-a_c(T)}{a_{HT}(T)} = -2e_{xx, sb}.$$

We decompose the total volume strain v_s in sb and nsb components, as done for the symmetrically-similar cases of leucite and D3C-THF,^{35, 53} with $v_s = \frac{V_{LT}-V_{HT}}{V_{HT}} = \frac{V_{LT}-V_c}{V_{HT}} + \frac{V_c-V_{HT}}{V_{HT}}$.

Since v_s is more than a few percent, it is necessary to use second order sb and nsb terms:

i) the symmetry breaking volume strain

$$v_\eta = \frac{V_{LT}-V_c}{V_{HT}} = (1 + e_{xx, sb})(1 + e_{xx, sb})(1 + e_{zz, sb}) - 1 \approx -3e_{xx, sb}^2$$

ii) the non-symmetry-breaking volume strain:

$$v_{CT} = \frac{V_c-V_{HT}}{V_{HT}} = (1 + e_{xx, nsb})(1 + e_{xx, nsb})(1 + e_{zz, nsb}) - 1 \approx 3e_{xx, nsb} + 3e_{xx, nsb}^2$$

$$v_s = v_{CT} + v_\eta = 3e_{xx, nsb} + 3e_{xx, nsb}^2 - 3e_{xx, sb}^2 = v_{CT} - 3e_{xx, sb}^2 \quad (1)$$

The typical values are $v_\eta = -0.0008$, $v_{CT} = -0.1022$ and $v_s = -0.103$.

The ferroelastic strain changes the shape of the unit cell, while an additional strain v_{CT} alters the volume. Some symmetry-breaking deformation related to η^2 may contribute to $e_{xx, nsb}$ in (1). However, the contribution to the volume strain v_s of the nsb component reaches $v_{CT} = -0.102$ for

$\eta = 0$, which is similar to the value reported for non-symmetry breaking CT²⁴ including the Rb_{0.73}MnFe compound.³⁹ Therefore the contribution of η^2 to v_s is mainly limited to v_η (Fig. 7c), which provides the affine relationship (1) between v_s and $e_{xx, sb}^2$ shown in Fig. 7d. However, since $v_\eta \ll v_s$, $v_s \approx v_{CT}$, and v_s is therefore mainly driven by the evolution of q , *i.e.* the fraction γ of CT state Mn^{III}Fe^{II}, transforming as the identity representation. Consequently, and the volume strain can be scaled to $v_s \propto (1 - \gamma) \propto (\frac{1-q}{2})$ as shown in Fig. 3b. The non-symmetry-breaking components play therefore an important role in the modification of various physical quantities, and we analyze hereafter the CT aspect responsible for the large v_s . It is well-known that such a simple Landau development is virtually never the correct potential in ferroelastics, as coupling to other degrees of freedom are often involved⁵⁴.

B. Landau development for the purely CT phase transition

We describe the CT transition, accounting for the transformation from Mn^{III}Fe^{II} to Mn^{II}Fe^{III} states, similar to CT-based transitions in CoFe or CoW systems.^{4-10, 46} These isostructural phase transitions are often of first order nature, due to the elastic cooperativity related to large volume change, as monitored through the fraction γ of Mn^{III}Fe^{II} state (Fig. 2) and the OP q describes the electronic instability and transforms as the identity representation of the $\bar{4}3m$ point group. For isostructural transitions associated with a totally symmetrical OP x , all powers of scalar x are allowed by symmetry in the thermodynamic potential, truncated here at the fourth-order term

$$F = A'x + \frac{1}{2}B'x^2 + \frac{1}{3}C'x^3 + \frac{1}{4}D'x^4$$

Substituting $q = x - \frac{1}{4}C'$ eliminates the third-order term, which limits the number of parameters in the potential, and allows for describing the symmetric evolution of q during the CT phase transition. Therefore, we use a potential similar to the one introduced by Chernyshov¹⁶ for describing non-symmetry-breaking spin-transition phenomena^{17, 55-57}:

$$F = Aq + \frac{1}{2}Bq^2 + \frac{1}{4}Cq^4 \quad (2)$$

with $A = -a_0(T - T_{CT})$, to stabilize the Mn^{III}Fe^{II} state ($q < 0$) below the CT transition temperature T_{CT} , $C > 0$ for stability and $B < 0$ to promote cooperativity. The stability of the different phases is found from $\frac{dF}{dq} = 0$ and $\frac{d^2F}{dq^2} > 0$. At $T = T_{CT}$ ($A = 0$) $q = 0$ is unstable, while the two symmetric stable solutions are $q = \pm \frac{B}{C}$. The evolution of the thermal equilibrium value of q with A provides the CT transition curve in Fig. 6b, from predominantly Mn^{II}Fe^{III} ($q > 0$, HT) to predominantly Mn^{III}Fe^{II} ($q < 0$ LT) phases. Due to $B < 0$, the thermal evolution of q has a characteristic "S shape",

corresponding to a thermal hysteresis inherent to first order CT-based phase transitions. The width of the coexistence region between the phases is $\Delta A_{CT} = 4C\left(\frac{-B}{3C}\right)^{\frac{3}{2}}$.

In the potentials used above, we considered independently the ferroelastic transition occurring at T_F , and the CT transition occurring at T_{CT} . These phase transitions may then occur simultaneously only at a single point of the phase diagram, where $T_F=T_{CT}$. This case does not correspond to a phase transition line between the $\text{Mn}^{\text{II}}\text{Fe}^{\text{III}}$ high symmetry and the $\text{Mn}^{\text{III}}\text{Fe}^{\text{II}}$ low symmetry phase, and for describing the phase transition, it is then necessary to consider the coupling between the order parameters q and η .

C. Linear quadratic coupling between q and η

For analyzing the evolution of the thermodynamic potential with q and η , we add to their individual contributions the coupling term of lowest order $Dq\eta^2$ always allowed by symmetry:

$$F = \frac{1}{2}a\eta^2 + \frac{1}{3}b\eta^3 + \frac{1}{4}c\eta^4 + Aq + \frac{1}{2}Bq^2 + \frac{1}{4}Cq^4 + Dq\eta^2 \quad (3)$$

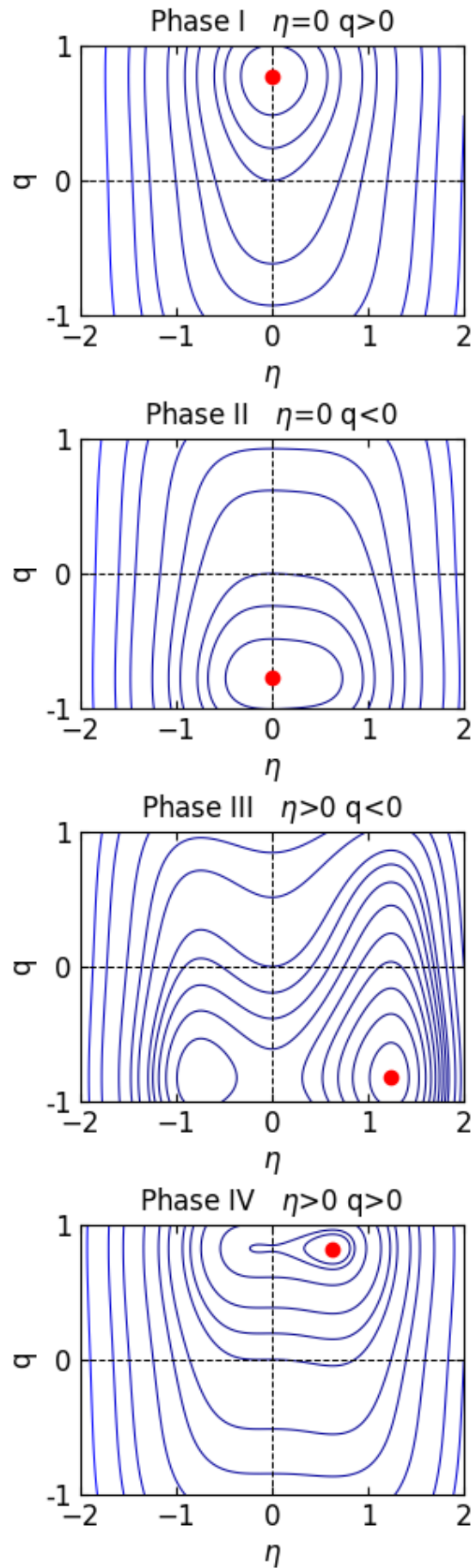
with $A = -a_0(T - T_{CT})$ and $a = -A - a_1$. $a_1 = -a_0(T_{CT} - T_F)$ measures the difference of temperature instability between the CT phase transition and the ferroelastic phase transition. Here again we consider the OP η as scalar, keeping in mind the 3 fold symmetry corresponding to the three domains elongated along z , y or x . We calculate, with the parameters of the potentials previously used for the purely ferroelastic and CT phase transitions, the evolution of this potential with A and a_1 and for different couplings D . The different phases that appear for different (a_1, A) are characterized by the equilibrium values of the OP corresponding to a minimum of the potential in the (q, η) space (Fig. 8) with $\frac{dF}{d\eta} = 0$, $\frac{dF}{dq} = 0$, $\frac{d^2F}{d\eta^2} > 0$, $\frac{d^2F}{dq^2} > 0$ and $\frac{d^2F}{dqd\eta} > 0$.

The phase space to explore with the parameters in Eq. (3) is limited and their values or ranges used for simulations are given in Table 1. As explained above, $b < 0$ is used for stabilizing the JT elongation, $B < 0$ to promote CT cooperativity, $c > 0$ and $C > 0$ for stability. $D > 0$ is also required to stabilize the LT and low symmetry phase ($q < 0, \eta > 0$). The relative change of parameters modifies the cooperative nature of the phase transitions but the qualitative features remain similar.

Parameter	a, a_1	$b/3$	$c/4$	$B/2$	$C/4$	D
value	-6 - 6	-2	3	-2, 2	3	0, 1, 2, 4

TAB. 1. Values and ranges of the parameters of the potential.

FIG. 8. Contour map of the potential (3) showing the evolution of the equilibrium positions indicated by the red dot in the (q, η) space and corresponding to phase I (HT), phase II, phase III (LT) and phase VI.



Phase I ($q > 0, \eta = 0$) corresponds to the HT and high symmetry $\text{Mn}^{\text{II}}\text{Fe}^{\text{III}}$ phase. With respect to phase I, phase II ($q < 0, \eta = 0$) corresponds to a non-symmetry-breaking CT phase transition, phase III ($q < 0, \eta > 0$) corresponds to the LT $\text{Mn}^{\text{III}}\text{Fe}^{\text{II}}$ phase with CT and ferroelastic distortion, and phase IV ($q > 0, \eta > 0$) corresponds to a purely ferroelastic distortion without CT. Without coupling ($D=0$), the stability conditions of the phases combine the results for the ferroelastic and CT transitions, which are presented in the (a_I, A) space (Fig. 9). The thermal evolution corresponds to a vertical line along A , with T increasing from $A>0$ to $A<0$. For the CT aspect, the phase transition line between the phases $q>0$ (I & IV) and $q<0$ (II & III) is centered at $A=0$ and a coexistence region ΔA_{CT} . For the ferroelastic aspect, the limit of stability of the high symmetry phase ($\eta = 0$) corresponds to $A = -a_1$, while the coexistence region is ΔA_F . For $D=0$, the four phases appear in the phase diagram (Fig. 9a) and coexist around $(a_I=0, A=0)$. However, the transition between phases I and III, corresponding to the HT and LT phases of RbMnFe , occurs only at this single point of the phase diagram $(a_I=0, A=0)$, which does not correspond to a phase transition line between phases I and III. The state $(q = 0, \eta = 0)$ is always unstable with $B<0$. By introducing in (3) a coupling term $D\neq 0$, the equilibrium $\eta = 0$ is found for: $a + 2Dq > 0$ and $q^2 > \frac{-B}{3C}$. For $\eta = 0$ the potential (3) corresponds to (2) for the isostructural CT transition from phase I to phase II, with a width of bistability ΔA_{CT} (Fig. 9b-e).

The non-zero solution is: $\eta = \frac{(-b + \sqrt{(b^2 - 4(2Dq + a)c})}{2c}$ for $A > -a_1 - \frac{b^2}{4c} + 2Dq$.

Writing (3): $F = \frac{1}{2}(a + 2Dq)\eta^2 + \frac{1}{3}b\eta^3 + \frac{1}{4}c\eta^4 + Aq + \frac{1}{2}Bq^2 + \frac{1}{4}Cq^4$ highlights that D renormalizes the η^2 coefficient, shifting T_F between phases II and III to $T_F' = T_F - \frac{2Dq}{a_0}$. $\eta \neq 0$ is then stable for $-a_1 > A + 2Dq$. Compared to the case without coupling, Fig. 9b shows that the coupling terms *i*) shifts the stability region along A between phases III and II for which $q<0$ by $-|2Dq|$, *ii*) shifts the stability region between phases I and IV for which $q>0$ by $+|2Dq|$. These transition lines are distorted because q is not constant in the phase diagram.

Writing (3): $F = \frac{1}{2}a\eta^2 + \frac{1}{3}b\eta^3 + \frac{1}{4}c\eta^4 + (A + D\eta^2)q + \frac{1}{2}Bq^2 + \frac{1}{4}Cq^4$ highlights that D shifts the III-IV transition temperature to $T_{CT'} = T_{CT} + \frac{D\eta^2}{a_0}$. As shown in Fig. 9b, this CT transition line is bent since η is not constant along the transition line. The I-III phase transition line is also affected by the coupling. For phase I the stability condition is $A < -a_1$ and for phase III it is $A > -a_1 - \frac{b^2}{4c} + 2Dq$ with $q<0$. The I-III hysteresis width increases then with the coupling strength D :

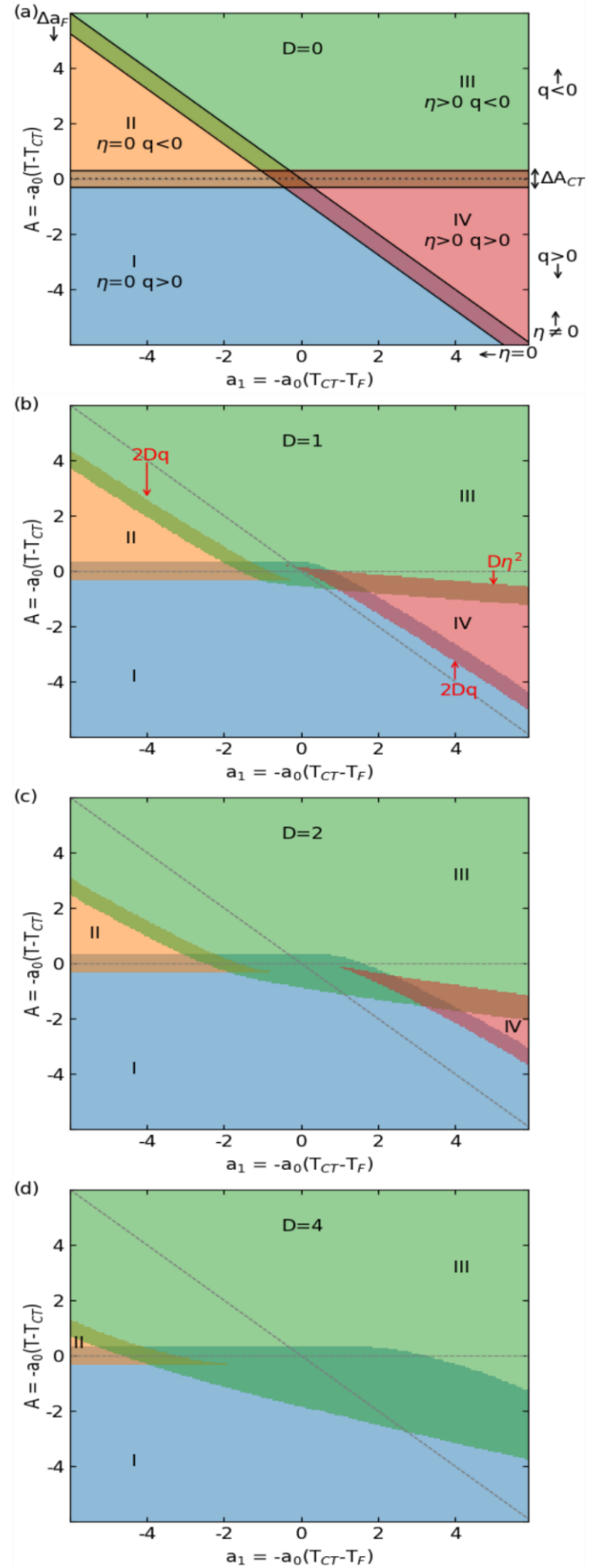
$$\Delta A = \frac{b^2}{4c} + |2Dq| \quad (4)$$

It is therefore the coupling term, which opens the I-III phase transition line and enlarges the bistability region of the phases. Except for the non-symmetry-breaking phase transition line I-II, which is unaffected, calculating the exact shifts of the phase transition lines is complex and without analytical solution, as the amplitude of both q and η depend on (A, a_I) . However, it is possible to compute the evolution of the potential and to find for each (A, a_I) the stable and metastable (η, q) values characterizing the different phases. The phase diagrams obtained in this way for different couplings $D=0, 1, 2, 4$ are shown in Fig. 9. Phases II and IV are destabilized by the coupling term, while phases I and III are stabilized over broader regions of the phase diagram. For discussing the phase diagram with a potential truncated at fourth order, it is sufficient to consider the $q\eta^2$ term of lowest order. Indeed, due to symmetry, including the $q^2\eta^2$ coupling term would simply balance the relative stability between phases where $\eta=0$ or $\eta\neq 0$ and shift the transition lines in one way or another depending on the sign of the coupling, while the $q^3\eta$ term is not allowed by symmetry. It is therefore the $q\eta^2$ term, which is responsible for the main features.

Fig. 6 shows the thermal evolutions of q and η for $D=0$ and $a_I = -5, 0, +5$. The behavior of q is unchanged as the CT transition is centered at $a_I=0$. The thermal evolution of η shifts with $a_I = a_0(T_{CT} - T_F)$, but since the OP are uncoupled, there is no discontinuous change of one OP when the other one changes during the transition. The hysteresis widths ΔA_{CT} and ΔA_F are chosen similar with the parameters used for pedagogical purpose. Fig. 10 shows at $a_I=0$ the effect of the coupling strengths D on the thermal evolution of the OP q and η . Due to the coupling, they change simultaneously and discontinuously during the phase transition. As indicated in equation (4), the width of the I-III hysteresis increases with the coupling strength D , as shown in the phase diagrams with the dark green area (Fig. 9) and becomes larger than ΔA_{CT} and ΔA_F . Fig. 11 shows the thermal evolution for $D=4$ and $a_I=0-6$. The width of the thermal hysteresis remains similar, but the hysteresis loops are shifted towards higher temperature when $a_I=a_0(T_{CT}-T_F)$ increases.

Fig. 12 compares the role of the degree of cooperativity of the CT aspect by showing the evolution with A at $a_I=0$ of the OP q and η when $D=2$ for $B=\pm 2$. The hysteresis is much larger for $B<0$ (cooperative CT transition) while for $B>0$ it is similar to the region of coexistence of the purely ferroelastic transition for $D=0$, even for large coupling. Indeed, $B<0$ constrains a discontinuous change between $q<0$ and $q>0$, with $q^2 > \frac{|B|}{3C}$, which increases the hysteresis width between phases I-III as $\Delta A = \frac{b^2}{4c} + |2Dq|$ (4). For $B>0$, q can approach 0 at the transition, which reduces ΔA . This key role of the cooperative nature of the CT agrees with the fact that many CT PBA, like CoFe or CoW systems,^{9, 10, 58, 59} exhibit first-order CT transition, without symmetry change. Using $B<0$ is more relevant in the model and corresponds to experimental observations like the broad thermal hysteresis.

FIG. 9. Phase diagrams in the (a_1, A) space. (a) $D=0$: the CT transition occurs at $A=0$ (dotted line), with an hysteresis width ΔA_{CT} . The ferroelastic transition occurs at $A=-a_1$ (thick line) with an hysteresis width ΔA_F . (b) shows the shift of the transition lines due to the coupling $D=1$, (c) for $D=2$ and (d) for $D=4$. The colors show the regions of stability and coexistence of the different phases. The dark green area marks the region of coexistence of the phases I and III. The parameters of the potential are those used in Figs. 6. For each panel the dotted lines correspond to $A=0$ and $A=-a_1$.



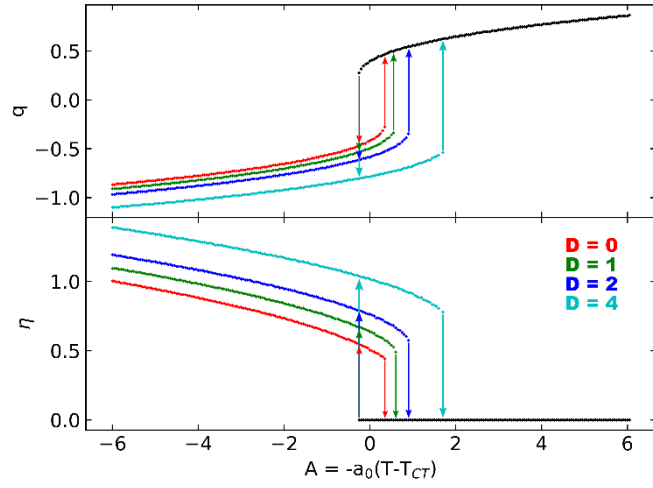


FIG. 10. Evolution of q and η with A for $a_I=0$. The hysteresis broadens with coupling strength D .

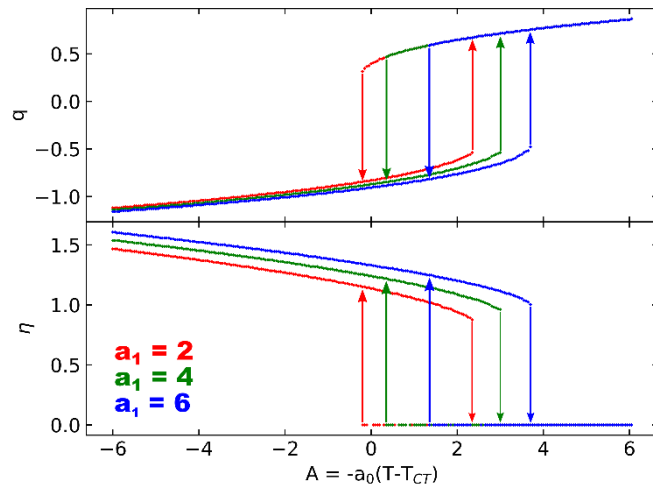


FIG. 11. Evolution of q and η with A for $D=4$. The hysteresis shifts with a_I , keeping similar width.

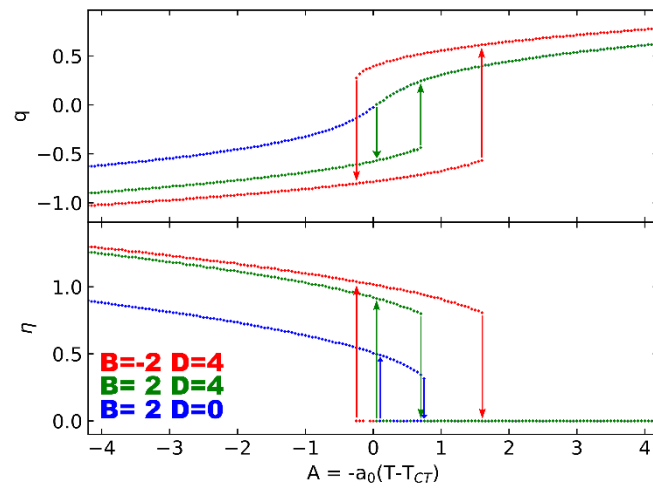


FIG. 12. Evolution with A for $a_I=2$ of q and η with D and B . The hysteresis is broader for cooperative CT transition ($B<0$). For $B>0$ the hysteresis is due to the ferroelastic transition, as q undergoes a crossover (blue).

IV. Discussion for RbMnFe systems

The experimental data reveal two types of changes in physical parameters, transforming like the non-symmetry-breaking OP q (or γ) or the symmetry-breaking OP η . The temperature dependences of the order parameters are summarized in Fig. 13a. The evolution of the $(\frac{1-q}{2})$ is obtained from the volume strain v_s , which is mainly driven by the CT (Fig. 3b), and the intensity of the IR band at 2150 cm^{-1} (Fig. 5), which provides an apparent tilt of the hysteresis branches during the phase nucleation due to the local nature of the probe. The relative evolution of η can be extracted from the width of the IR band in the LT phase (Fig. 5), the splitting of the lattice parameters (Fig. 3a) and the splitting of the Mn-N bond lengths (Fig. 5).

The results from the Landau model in equation (3) shown in Fig. 13b are in qualitative agreement and highlight the role of the coupling term in the broadening of the thermal hysteresis, as well as the coupled and discontinuous evolution of the order parameters (q, η) during the phase transition. However, contrary to experiments, the model exhibits some temperature dependence of the OP. This shortcoming may be due to developing the expansion of the thermodynamic potential in minimal form and up to 4th order terms only. For the same reason, the non-symmetry-breaking transition does not exhibit Heaviside step-like change of CT observed in many systems from HT phase where $q = 1$ to LT phase where $q = -1$.^{9, 10, 58, 59} Instead, our model provides some pre-transitional variations, also obtained with other models describing the CT transition.^{29, 30} Our theoretical model can mimic various experimental observations, and it is the symmetry-allowed lowest-order coupling, $Dq\eta^2$, which is responsible for key features in the phase diagram *i*) opening a phase transition line between phases I (HT) and III (LT), *ii*) broadening the width of the thermal hysteresis, *iii*) driving simultaneous changes of the OP.

For a deeper understanding of the processes coming into play, the nature of the coupling D introduced phenomenologically, and stabilizing a ferroelastic distortion in the $\text{Mn}^{\text{III}}\text{Fe}^{\text{II}}$ LT phase, should be discussed. Compared to the cubic $\text{Mn}^{\text{II}}\text{Fe}^{\text{III}}$ state with 2 electrons in the e_g orbitals, the LT $\text{Mn}^{\text{III}}\text{Fe}^{\text{II}}$ state is more bonding as there is a single electron on the e_g -like anti-bonding orbitals, which results in an average shortening of the Mn-N and Fe-C bonds and a decrease of the volume of the MnN_6 and FeC_6 octahedra. The change of electronic state from $\text{Mn}^{\text{II}}\text{Fe}^{\text{III}}$ to $\text{Mn}^{\text{III}}\text{Fe}^{\text{II}}$ results in a non-symmetry-breaking change q of the population of the e_g orbitals. However, the $\text{Mn}^{\text{III}}\text{Fe}^{\text{II}}$ state is stabilized by a symmetry-breaking structural reorganization, which lifts the degeneracy between the $\text{Mn}(dx^2-y^2)$ and $\text{Mn}(dz^2)$ states, stabilizing the occupied dz^2 orbital. The corresponding JT distortion, leading to shorter Mn-N bonds along x and y compared to z , transforms like the bidimensional E representation of the HT point group $\bar{4}3m$.

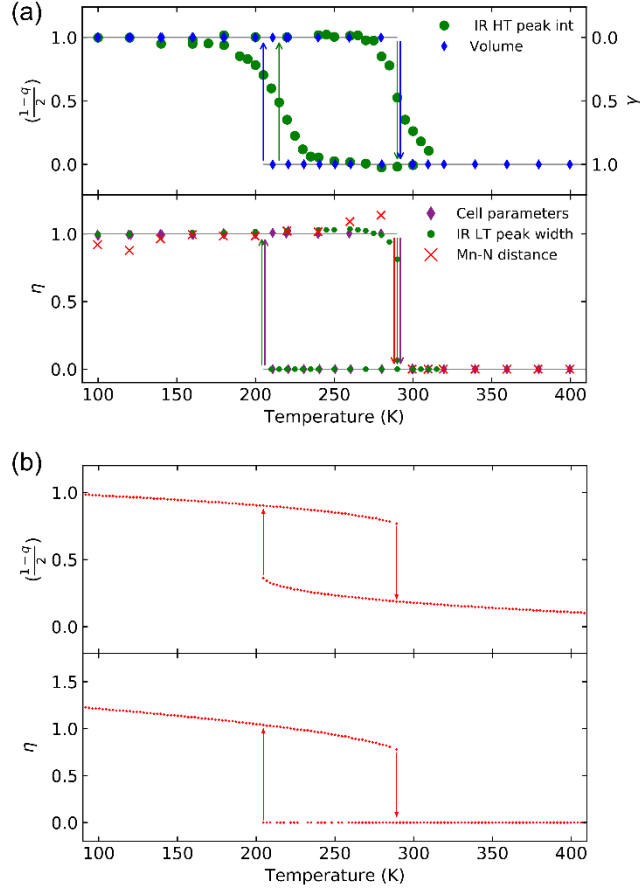


FIG. 13. Thermal evolution of $\left(\frac{1-q}{2}\right)$ or γ (right axis), and η^2 . (a) Experimental data. (b) Theoretical results from the potentials (3) for $D=4$ scaled to temperature. The elastic couplings broaden the hysteresis and limit the thermal dependence of the order parameters (η is normalized to 1 for clarity).

This strong coupling between electronic and structural reorganization is the microscopic origin of the $q\eta^2$ coupling as the CT (q) is stabilized by the JT distortion (η).⁴³ The changes of q and η occur in a cooperative way within the 3D polymeric lattice, mainly due to the elastic cost, and are responsible for lattice strains. Like the chicken or the egg causality dilemma, the relative role of non-symmetry-breaking (q) and the symmetry-breaking (η) changes may be questioned. However, the fact that the isostructural compounds $\text{Rb}_{0.73}\text{MnFe}$ undergoes the $\text{Mn}^{\text{II}}\text{Fe}^{\text{III}}$ to $\text{Mn}^{\text{III}}\text{Fe}^{\text{II}}$ CT phase transition without symmetry-breaking,³⁹ like many others cyano-bridged CT metal complexes,^{9, 10, 58, 59} suggests that the ferroelastic strain may be regarded as driven by the CT rather than driving. In these volume-changing phase transitions, where molecular-based deformations propagate at the macroscopic scale, elastic energy terms must be considered. In the case of conventional cubic-tetragonal ferroelastic distortions elastic terms due to symmetry-breaking (v_η) contribute to the potential. On the other hand, in the case of the non-symmetry-breaking CT phase transition, only

q , or v_{CT} , are considered due to the change in the bonding nature of the lattice accompanying the change of electronic state.^{3, 60, 61} For RbMnFe, during the phase transition between LT and HT phases, both instabilities related to structural deformations of different symmetries contribute to then to the total volume strain ($v_s = v_\eta + v_{CT}$). Since v_s and q transform as the identity representation A_1 and η as the representation E, we add the symmetry-allowed elastic terms to the ferroelastic and CT potentials:

$$F = \frac{1}{2}a\eta^2 + \frac{1}{3}b\eta^3 + \frac{1}{4}c\eta^4 + Aq + \frac{1}{2}Bq^2 + \frac{1}{4}Cq^4 + \lambda_\eta v_s \eta^2 + \lambda_q v_s \left(\frac{1-q}{2}\right) + \frac{1}{2}C_s^0 v_s^2 \quad (5)$$

$\frac{1}{2}C_s^0 v_s^2$ is the elastic energy related the total volume strain v_s , $\lambda_\eta v_s \eta^2$ is the elastic coupling to v_s of the ferroelastic OP and is zero in the HT phase, $\lambda_q v_s \left(\frac{1-q}{2}\right)$ is the elastic coupling to v_s of the CT conversion scaling as $\left(\frac{1-q}{2}\right)$ to be zero in the HT phase and similar to the elastic energy introduced for volume-changing spin-crossover materials.⁶²

Equation (5) provides the well-known relationship between elastic energy and coupling energy:

$$\lambda_\eta v_s \eta^2 + \lambda_q v_s \left(\frac{1-q}{2}\right) = -C_s^0 v_s^2 = -2 \left(\frac{1}{2}C_s^0 v_s^2\right)$$

where the energy gain due to the elastic coupling is twice larger than the elastic energy cost.³²

The equilibrium value of v_s minimizing the potential (5) is:

$$v_s = -\frac{[\lambda_q \left(\frac{1-q}{2}\right) + \lambda_\eta \eta^2]}{C_s^0} = -\frac{\lambda_q}{C_s^0} \left(\frac{1-q}{2}\right) - K e_{xx, sb}^2 \quad (6)$$

This affine relationship between $e_{xx, sb}^2$ (or η^2) and v_s agrees with equation (1) found from the non-symmetry-breaking and symmetry-breaking components of the deformations (see Fig. 7d).

Substituting v_s in equation (5) renormalizes some coefficients of the Landau expansion:

$$F = \frac{1}{2} \left(a - \frac{\lambda_\eta \lambda_q}{C_s^0}\right) \eta^2 + \frac{1}{3} b \eta^3 + \frac{1}{4} \left(c - \frac{\lambda_\eta^2}{2C_s^0}\right) \eta^4 + \left(A + \frac{\lambda_q^2}{4C_s^0}\right) q + \frac{1}{2} \left(B - \frac{\lambda_q^2}{8C_s^0}\right) q^2 + \frac{1}{4} C q^4 + \left(\frac{\lambda_\eta \lambda_q}{2C_s^0}\right) q \eta^2 \quad (7)$$

It appears then that it is the elastic couplings of each OP to the volume strain, which lead to an effective linear-quadratic coupling strength D between the order parameters, related to the elastic constant C_s^0 , with $D = \frac{\lambda_\eta \lambda_q}{2C_s^0}$. The renormalization shifts the temperatures T_{CT} and T_F .

Regarding the family of $\text{Rb}_x\text{Mn}[\text{Fe}(\text{CN})_6]_{(x+2)/3} \cdot z\text{H}_2\text{O}$ materials, our model is sufficiently flexible to map several scenarios found experimentally. In the case of the RbMnFe system The linear coupling of $\left(\frac{1-q}{2}\right)$ to v_s also affect the CT instability, making the q^2 coefficient $\left(B - \frac{\lambda_q^2}{8C_s^0}\right)$ more negative and broadening the CT hysteresis width ΔA_{CT} . This explains why the thermal hysteresis

is of similar order for the $\text{Rb}_{0.73}\text{MnFe}$ compound undergoing non-symmetry breaking CT-based phase transition.³⁹ The broadening of the thermal hysteresis with the coupling strength due to the elastic coupling (Fig. 10) is similar to the broadening observed under chemical pressure. Indeed, when the fraction x of Rb alkali changes from 1 to 0.64, the hysteresis width expands from 73 K to 138 K.²⁷ The Rb concentration x allows then for a chemical control of the coupling strength, since the Rb acts as a spacer within the lattice. On the other hand, the thermal shift of the hysteresis, on the order of 0.026 K/bar⁶³ under hydrostatic pressure, is similar to the shift with $a_I = a_0(T_{CT} - T_F)$ shown in Fig. 11. Indeed, pressure stabilizes lower volume states towards higher temperature, but the volume strain v_{CT} due to CT is much larger than the volume strain v_η due to the ferroelastic transition. Consequently, T_{CT} increases more with increasing pressure than T_F and a_I is then analogous to pressure. Our theoretical model can also be used to describe I-II non-symmetry-breaking CT transitions observed in various materials belonging to the family of cyano-bridged CT metal complexes,^{9, 10, 58, 59} which may be of first-order ($B < 0$) or crossover ($B > 0$) nature. The model also describes ferroelastic phase transitions in PBA,⁴ without CT, analogous to the I-IV or II-III phase transitions, and it also predicts sequences of CT and symmetry-breaking phase transitions (I-II-III or I-IV-III) not reported yet experimentally to our knowledge in PBA.

V. Generalization of the model to other systems

The Landau model discussed here, where a non-symmetry-breaking electronic instability related to an OP q may couple to a symmetry-breaking instability η in a linear-quadratic way, applies to various systems. For example, it can describe the phase transition reported in few spin-crossover materials, for which the non-symmetry-breaking change of spin state (q) couples to a ferroelastic distortions (η) and result in a broad thermal hysteresis.^{21, 64-66} The model also account for totally symmetric changes of electronic state in one-dimensional organic conductors coupled to ferroelastic distortion.⁶⁷ The phase diagram in Fig. 9d is also similar to the one of V_2O_3 , exhibiting a non-symmetry-breaking phase transition I-II between the metal trigonal phase and the Mott insulator trigonal phase, and symmetry-breaking transition lines I-III or II-III between these phases and the monoclinic Mott insulator phase.² This phase diagram is also similar to the one of TTF-CA undergoing a neutral-ionic transition,^{15, 68} where a non-symmetry-breaking CT between electron donor and acceptor molecules and a ferroelectric symmetry-breaking phase transition can be concomitant (I-III) or sequential (I-II and II-III). The Ti_3O_5 material is another type of system, which undergoes a sequence of phase transitions with an orthorhombic ($Cmcm$) to monoclinic ($C2/m$) ferroelastic transition around 500 K between two metallic phases and a non-symmetry-breaking phase transition around 450 K towards a semiconducting phase ($C2/m$).⁶⁹ This

corresponds to the sequence of phases I-IV-III in our model. The non-symmetry-breaking IV-III semiconducting-to-metallic phase transition is associated with a wide domain of bistability due to large volume strain, allowing for reversible photoswitching within the hysteresis.¹³

These phase diagrams or sequences of phases are also similar to the gas-liquid-solid one, with three transition lines meeting at a triple point. The phase transition I-II is the non-symmetry breaking one (gas-liquid-like) related to a discontinuous change of q , equivalent to density. The phase transition II-III is the symmetry-breaking one (liquid-solid-like) related to a change from $\eta=0$ to $\eta\neq 0$. During the phase transition I-III (gas-solid-like) q and η change in a coupled way. It is important to underline that for the different examples mentioned above, the non-symmetry breaking electronic instability (Mott transition, semiconducting-metallic, neutral-ionic transition, spin transition, CT...) originates from a relative change of the occupation (q) of anti-bonding electronic states, which, by coupling linearly to v_s , drives elastically cooperative phase transition with spectacular changes of various types of physical properties. When symmetry-breaking components come into play, the volume strain may also couple to the symmetry-breaking OP through the $q\eta^2$ term and the non-symmetry-breaking and symmetry-breaking phase transitions may be concomitant or sequential.

VI. Conclusion

We used the Landau theory to study phase transitions where an electronic instability, related to a non-symmetry-breaking OP q , and a symmetry-breaking instability, related to an OP η may occur simultaneously due to their elastic coupling $q\eta^2$. The phase diagrams obtained highlight the importance of non-symmetry-breaking changes related to electronic instabilities, strongly changing the bonding nature of the lattice, and responsible for large volume strain that may drive cooperative phase transitions. This general model, taking into account the coupling between symmetry-breaking and non-symmetry-breaking components is sufficiently flexible to describe phase diagrams in various types of materials.

Acknowledgement

This project was carried out in the frame of the IM-LED LIA (CNRS) and a JSPS Grant-in-Aid for Scientific Research (A) 20H00369 and JSPS KAKENHI 16H06521 Coordination Asymmetry. The authors gratefully acknowledge Agence Nationale de la Recherche for financial support undergrant ANR-16-CE30-0018, ANR-19-CE30-0004 and University Rennes 1 for funding. We thank H. Cailleau for scientific discussions.

References

1. L. Landau, *Ukr. J. Phys.* **53**, 25-35 (2008).
2. D. B. McWhan, A. Menth, J. P. Remeika, W. F. Brinkman and T. M. Rice, *Physical Review B* **7** (5), 1920-1931 (1973).
3. H. Spiering, K. Boukheddaden, J. Linares and F. Varret, *Physical Review B* **70**, 184106 (2004).
4. A. Bleuzen, J.-D. Cafun, A. Bachschmidt, M. Verdaguer, P. Münsch, F. Baudelet and J.-P. Itié, *The Journal of Physical Chemistry C* **112** (45), 17709-17715 (2008).
5. N. Shimamoto, S. Ohkoshi, O. Sato and K. Hashimoto, *Inorganic Chemistry* **41** (4), 678-684 (2002).
6. N. Ozaki, H. Tokoro, Y. Hamada, A. Namai, T. Matsuda, S. Kaneko and S. Ohkoshi, *Advanced Functional Materials* **22** (10), 2089-2093 (2012).
7. V. Escax, A. Bleuzen, J. P. Itié, P. Munsch, F. Varret and M. Verdaguer, *The Journal of Physical Chemistry B* **107** (20), 4763-4767 (2003).
8. V. Escax, A. Bleuzen, C. Cartier dit Moulin, F. Villain, A. Goujon, F. Varret and M. Verdaguer, *Journal of the American Chemical Society* **123** (50), 12536-12543 (2001).
9. D. Aguila, Y. Prado, E. S. Koumoussi, C. Mathoniere and R. Clerac, *Chemical Society Reviews* **45** (1), 203-224 (2016).
10. A. C. Felts, M. J. Andrus, E. S. Knowles, P. A. Quintero, A. R. Ahir, O. N. Risset, C. H. Li, I. Maurin, G. J. Halder, K. A. Abboud, M. W. Meisel and D. R. Talham, *The Journal of Physical Chemistry C* **120** (10), 5420-5429 (2016).
11. H. Tokoro, T. Matsuda, K. Hashimoto and S. Ohkoshi, *Journal of Applied Physics* **97** (10), 10M508 (2005).
12. O. Sato, *Nat Chem* **8** (7), 644-656 (2016).
13. S. Ohkoshi, Y. Tsunobuchi, T. Matsuda, K. Hashimoto, A. Namai, F. Hakoe and H. Tokoro, *Nat Chem* **2** (7), 539-545 (2010).
14. N. A. Spaldin and M. Fiebig, *Science* **309** (5733), 391-392 (2005).
15. M. Buron-Le Cointe, E. Collet, B. Toudic, P. Czarnecki and H. Cailleau, *Crystals* **7** (10), 285 (2017).
16. D. Chernyshov, H.-B. Bürgi, M. Hostettler and K. W. Törnroos, *Physical Review B* **70**, 094116 (2004).
17. H. Watanabe, K. Tanaka, N. Bréfuel, H. Cailleau, J.-F. Létard, S. Ravy, P. Fertey, M. Nishino, S. Miyashita and E. Collet, *Physical Review B* **93**, 014419 (2016).
18. M. Iwata, H. Orihara and Y. Ishibashi, *Journal of the Physical Society of Japan* **66** (4), 1205-1209 (1997).
19. E. K. Salje and M. A. Carpenter, *J Phys Condens Matter* **23** (46), 462202 (2011).
20. Y. M. Gufan, *Sov. Phys. - Solid. State* **22**, 951 (1980).
21. V. B. Jakobsen, E. Trzop, L. C. Gavin, E. Dobbelaar, S. Chikara, X. Ding, K. Esien, H. Müller-Bunz, S. Felton, V. S. Zapf, E. Collet, M. A. Carpenter and G. G. Morgan, *Angewandte Chemie International Edition*, doi:10.1002/anie.202003041.
22. O. Sato, T. Iyoda, A. Fujishima and K. Hashimoto, *Science* **272** (5262), 704-705 (1996).
23. S. Ohkoshi and H. Tokoro, *Accounts of Chemical Research* **45** (10), 1749-1758 (2012).
24. C. Cartier dit Moulin, F. Villain, A. Bleuzen, M.-A. Arrio, P. Sainctavit, C. Lomenech, V. Escax, F. Baudelet, E. Dartyge, J.-J. Gallet and M. Verdaguer, *Journal of the American Chemical Society* **122** (28), 6653-6658 (2000).
25. O. N. Risset, P. A. Quintero, T. V. Brinzari, M. J. Andrus, M. W. Lufaso, M. W. Meisel and D. R. Talham, *Journal of the American Chemical Society* **136** (44), 15660-15669 (2014).
26. M. Verdaguer, A. Bleuzen, V. Marvaud, J. Vaissermann, M. Seuleiman, C. Desplanches, A. Sculler, C. Train, R. Garde, G. Gelly, C. Lomenech, I. Rosenman, P. Veillet, C. Cartier and F. Villain, *Coordination Chemistry Reviews* **190-192**, 1023-1047 (1999).
27. H. Tokoro, S. Miyashita, K. Hashimoto and S. Ohkoshi, *Physical Review B* **73**, 172415 (2006).
28. H. Tokoro and S. Ohkoshi, *Bulletin of the Chemical Society of Japan* **88** (2), 227-239 (2015).
29. E. D. Loutete-Dangui, E. Codjovi, H. Tokoro, P. R. Dahoo, S. Ohkoshi and K. Boukheddaden, *Physical Review B* **78**, 014303 (2008).
30. H. Tokoro, A. Namai, M. Yoshikiyo, R. Fujiwara, K. Chiba and S. Ohkoshi, *Sci Rep* **8** (1), 63 (2018).
31. S. C. Tarantino, M. Giannini, M. A. Carpenter and M. Zema, *Iucrj* **3**, 354-366 (2016).
32. M. A. Carpenter and E. K. Salje, *Eur. J. Mineral.* **10**, 693 (1998).
33. V. Janovec, V. Dvořák and J. Petzelt, *Czechoslovak Journal of Physics B* **25** (12), 1362-1396 (1975).
34. T. Yamanaka, T. Mine, S. Asogawa and Y. Nakamoto, *Physical Review B* **80**, 134120 (2009).

35. D. C. Palmer, E. K. H. Salje and W. W. Schmahl, *Physics and Chemistry of Minerals* **16** (7), 714 (1989).
36. J. D. Axe and Y. Yamada, *Physical Review B* **24** (5), 2567-2569 (1981).
37. J. Luzon, M. Castro, E. J. M. Vertelman, R. Y. N. Gengler, P. J. van Koningsbruggen, O. Molodtsova, M. Knupfer, P. Rudolf, P. H. M. van Loosdrecht and R. Broer, *The Journal of Physical Chemistry A* **112** (25), 5742-5748 (2008).
38. H. Tokoro, T. Matsuda, T. Nuida, Y. Moritomo, K. Ohoyama, E. D. L. Dangui, K. Boukheddaden and S. Ohkoshi, *Chem Mater* **20** (2), 423-428 (2008).
39. S. Ohkoshi, T. Matsuda, H. Tokoro and K. Hashimoto, *Chem Mater* **17** (1), 81-84 (2005).
40. Y. Moritomo, K. Kato, A. Kuriki, M. Takata, M. Sakata, H. Tokoro, S. Ohkoshi and K. Hashimoto, *Journal of the Physical Society of Japan* **71** (9), 2078-2081 (2002).
41. H. Tokoro, K. Hashimoto and S. Ohkoshi, *J Magn Magn Mater* **310** (2), 1422-1428 (2007).
42. S. Ohkoshi, H. Tokoro, M. Utsunomiya, M. Mizuno, M. Abe and K. Hashimoto, *The Journal of Physical Chemistry B* **106** (10), 2423-2425 (2002).
43. H. Tokoro, S. Ohkoshi, T. Matsuda and K. Hashimoto, *Inorganic Chemistry* **43** (17), 5231-5236 (2004).
44. H. Tokoro, S. Ohkoshi and K. Hashimoto, *Applied Physics Letters* **82** (8), 1245-1247 (2003).
45. K. Kato, Y. Moritomo, M. Takata, M. Sakata, M. Umekawa, N. Hamada, S. Ohkoshi, H. Tokoro and K. Hashimoto, *Physical Review Letters* **91**, 255502 (2003).
46. H. Tokoro, K. Nakagawa, K. Imoto, F. Hakoe and S. Ohkoshi, *Chem Mater* **24** (7), 1324-1330 (2012).
47. V. Janovec and J. Privratska, *International Tables for Crystallography D*, 449-505 (2006).
48. E. K. Salje, *Phase Transitions in Ferroelastic and Co-elastic Crystals*. (Cambridge University Press, Cambridge, 1991).
49. P. Toledano, M. M. Fejer and B. A. Auld, *Physical Review B* **27** (9), 5717-5746 (1983).
50. P. W. Anderson and E. I. Blount, *Physical Review Letters* **14** (7), 217-219 (1965).
51. M. A. Fradkin, *Phys Rev B Condens Matter* **50** (22), 16326-16339 (1994).
52. M. A. Carpenter, E. K. H. Salje and A. Graeme-Barber, *Eur. J. Mineral.* **10**, 621-691 (1998).
53. K. Knorr and W. Depmeier, *J Solid State Chem* **137** (1), 87-93 (1998).
54. E. K. H. Salje, *Annual Review of Materials Research* **42** (1), 265-283 (2012).
55. M. Buron-Le Cointe, J. Hébert, C. Baldé, N. Moisan, L. Toupet, P. Guionneau, J. F. Létard, E. Freysz, H. Cailleau and E. Collet, *Physical Review B* **85**, 064114 (2012).
56. A. Slimani, K. Boukheddaden and K. Yamashita, *Physical Review B* **92**, 014111 (2015).
57. M. A. Halcrow, *Spin-crossover materials : properties and applications*. (Wiley, 2013).
58. J. Mercuro, Y. Li, E. Pardo, O. Risset, M. Seuleiman, H. Rousseliere, R. Lescouezec and M. Julve, *Chem Commun* **46** (47), 8995-8997 (2010).
59. E. S. Koumoussi, I.-R. Jeon, Q. Gao, P. Dechambenoit, D. N. Woodruff, P. Merzeau, L. Buisson, X. Jia, D. Li, F. Volatron, C. Mathonière and R. Clérac, *Journal of the American Chemical Society* **136** (44), 15461-15464 (2014).
60. R. Bertoni, M. Lorenc, H. Cailleau, A. Tissot, J. Laisney, M. L. Boillot, L. Stoleriu, A. Stancu, C. Enachescu and E. Collet, *Nat Mater* **15** (6), 606-610 (2016).
61. R. Traiche, M. Sy, H. Oubouchou, G. Bouchez, F. Varret and K. Boukheddaden, *The Journal of Physical Chemistry C* **121** (21), 11700-11708 (2017).
62. V. Ksenofontov, H. Spiering, A. Schreiner, G. Levchenko, H. A. Goodwin and P. Gülich, *Journal of Physics and Chemistry of Solids* **60** (3), 393-399 (1999).
63. K. Boukheddaden, E. D. Loutete-Dangui, E. Codjovi, M. Castro, J. A. Rodríguez-Velamazán, S. Ohkoshi, H. Tokoro, M. Koubaa, Y. Abid and F. Varret, *Journal of Applied Physics* **109** (1), 013520 (2011).
64. C. Mariette, E. Trzop, J.-Y. Mevellec, A. Boucekkine, A. Ghoufi, G. Maurin, E. Collet, M. C. Muñoz, J. A. Real and B. Toudic, *Physical Review B* **103**, 134103 (2020).
65. E. Tailleux, M. Marchivie, P. Negrier, D. Denux, S. Massip, D. Mondieig, G. Chastanet and P. Guionneau, *Crystengcomm* **21** (41), 6246-6251 (2019).
66. M. H. Lemée-Cailleau, C. Ecolivet, B. Ouladdiaf, F. Moussa, J. Jeftic and J. F. Létard, *J Magn Magn Mater* **310** (2, Part 2), 1792-1793 (2007).
67. O. Jeannin, E. W. Reinheimer, P. Foury-Leylekian, J. P. Pouget, P. Auban-Senzier, E. Trzop, E. Collet and M. Fourmigue, *Iucrj* **5**, 361-372 (2018).
68. M. H. Lemée-Cailleau, M. Le Cointe, H. Cailleau, T. Luty, F. Moussa, J. Roos, D. Brinkmann, B. Toudic, C. Ayache and N. Karl, *Physical Review Letters* **79** (9), 1690-1693 (1997).
69. M. Onoda, *J Solid State Chem* **136** (1), 67-73 (1998).